

An Efficient Cervical Whole Slide Image Analysis Framework Based on Multi-scale Semantic and Location Deep Features

Ziquan Wei^{a,b,1}, Shenghua Cheng^{a,b,1,*}, Junbo Hu^c, Li Chen^d, Shaoqun Zeng^{a,b}, Xiuli Liu^{a,b,*}

^a Collaborative Innovation Center for Biomedical Engineering, Wuhan National Laboratory for Optoelectronics-Huazhong University of Science and Technology, Wuhan, Hubei 430074, China

^b Britton Chance Center and MOE Key Laboratory for Biomedical Photonics, School of Engineering Sciences, Huazhong University of Science and Technology, Wuhan, Hubei 430074, China

^c Department of Pathology, Maternal and Child Hospital of Hubei Province, Tongji Medical College, Huazhong University of Science and Technology, Wuhan, Hubei 430070, China

^d Department of Clinical Laboratory, Tongji Hospital, Tongji Medical College, Huazhong University of Science and Technology, Wuhan, Hubei 430030, China

ARTICLE INFO

Article history:

Keywords: Whole slide image analysis, Deep learning, Cervical cancer screening, Improved YOLO Network

ABSTRACT

Digital gigapixel whole slide image (WSI) is widely used in clinical diagnosis, and automated WSI analysis is key for computer-aided diagnosis. Currently, analyzing the integrated descriptor of probabilities or feature maps from massive local patches encoded by ResNet classifier is the main manner for WSI-level prediction. Feature representations of the sparse and tiny lesion cells in cervical slides, however, are still challenging, while the unused location representations are available to supply the semantics classification. This study designs a novel and efficient framework with a new module InCNet constructed lightweight model YOLCO (You Only Look Cytology Once). It directly extracts feature inside the single cell (cluster) instead of the traditional way that from image tile with a fixed size. The InCNet (Inline Connection Network) enriches the multi-scale connectivity without efficiency loss. The proposal allows the input size enlarged to megapixel that can stitch the WSI by the average repeats decreased from $10^3 \sim 10^4$ to $10^1 \sim 10^2$ for collecting features and predictions at two scales. Based on Transformer for classifying the integrated multi-scale multi-task WSI features, the experimental results appear 0.872 AUC score better than the best conventional model on our dataset ($n=2,019$) from four scanners. The code is available in this github [link](#), where the deployment version has the speed ~ 70 s/WSI.

© 2022 Elsevier B. V. All rights reserved.

1. Introduction

1.1. Background

Cervix cancer is one of the most common and dangerous diseases with mortality, more than 0.34 million cases, which is higher than half of the incidence, about 0.6 million cases, in 2020 (world, all ages) (Sung et al. (2021)). Furthermore, the 5-year survival rate of cervical cancer is as high as 92% (Saslow et al. (2012)) if detected early, and hence it is significant that enhancing the accuracy of cervical cancer screening. The usage of

*Corresponding author: Shenghua Cheng, Xiuli Liu.

e-mail: wzquan142857@hust.edu.cn (Ziquan Wei), chengshen@hust.edu.cn (Shenghua Cheng), cqjbhu@163.com (Junbo Hu), chengliisme@126.com (Li Chen), sqzeng@mail.hust.edu.cn (Shaoqun Zeng), xlliu@mail.hust.edu.cn (Xiuli Liu)

¹ authors have the equal contribution.

artificial intelligence (AI) assistance for cytopathology screening is valid and commonly based on the signal that is scanned and loaded into the computer, where the digital signal captured from the glass slide is called as whole slide image (WSI). AI assistance can directly guide pathologists starting at the recommended skeptical lesion area in the computer-aided diagnosis (CAD), instead of the traditional labour-intensive screening on the gigapixel region of interest in a real glass slide or a WSI. As such, automatically analyzing WSI and predicting at the patch-level is an active topic in the CAD.

For the automated screening, the cervical WSI with the liquid-based cytology test (LCT) is widely adopted by the medical community, which is an effective technique for aiding pathologists and computers in locating abnormal cells (Davey *et al.* (2006)). Especially, the top skeptical abnormal cells are normally considered to represent the WSI to avoid the analysis for all cells, which is the custom of human experts against the enormous count of cervical cells. Since the cytopathological diagnosis is built on the appearance and the comparison of individual abnormal cells or cells clusters under experience in the WSI along with the global information of background (Nayar and Wilbur (2017)), formulating the problem to tasks at cell level or patch-level is natural for the CAD. Unavoidably, the expert also applies the multiple dimensional features like the artificial area or the bacteria infection with the relevance between abnormal cells at the WSI-level. Consequently, researches are divided into two main directions, focusing on the local prediction only, which is the most of recent works for cervical CAD, and completing it with a WSI-level determination, which is the aim of this work to automatically analyze the LCT WSI from Papanicolaou (PAP) smears.

1.2. Related Works

Since the deep learning era has significantly improved the performance in various biomedical applications, the convolutional neural network (CNN) shows validity to predict cervical abnormal cells classification and segmentation at the patch-level. Many explorations based on deep learning have been studied in recent years. Emerging works are trying to take advantage of CNN to improve the segmentation accuracy of cytoplasm and nuclei (Tareef *et al.* (2017); Lu *et al.* (2016)). While the classification accuracy dropped with the segmentation error (Zhang *et al.* (2017)). Then, DeepPap (Zhang *et al.* (2017)) earlier applied CNN to classify cervical cells without the prior segmentation and hand-crafted features, which shows superior performances on the Herlev Pap smear dataset (Jantzen *et al.* (2005)) and HEMLBC (H&E stained manual LBC) dataset (Zhang *et al.* (2014)), but since the random-view aggregation and multiple crop testing are parts of the inference, it is very time-consuming. To further improve the performance of classification, Dong *et al.* (2020) proposed the combination of InceptionV3 and artificial features to explicitly adapt with the cervical cell domain knowledge, and achieved an accuracy of more than 98% on the Herlev dataset.

Along with the development of object detecting function that able to bound and classify cervical cells, contemporarily, a customized YOLOv3 with an additional task-specific classifier head is proposed by Xiang *et al.* (2020), which achieved

a mean average precision of 63.4% on a 10-class dataset consists of 1,014 annotated cervical cell images with the size of 4000×3000 . To deal with the data limitation, the customized Faster RCNN named Comparison detector is proposed by Liang *et al.* (2021) achieved an improvement against with the baseline whether on their larger dataset or their smaller dataset. Their total dataset has 48,587 instances belong to 7,410 cervical microscopical images scanned by one device. Additionally, over 16,000 TCT (Thinprep Cytologic Test) images as the train-val set were collected in Tan *et al.* (2021), as well as 290 larger regions of interest (ROIs) as the test set, which TCT smear is rare on cervical automatic diagnosis studies. Authors evaluated Faster RCNN enormously and randomly sampling of small images on the test set and achieved an appealing performance.

Furthermore, the cervical WSI has several gigapixels scanned at $20\times$ magnification ($0.24\mu\text{m}/\text{pixel}$), and hundreds of them can be counted of pixels equal to the entire ImageNet dataset. However, it can generate hundreds of thousands of small images that are contextual but unlabeled. For example, unlabeled foreground pixels outnumber labeled pixels of one slide 201 to 1 in our dataset. Lacking the learnable pixels is the physical property based on the sparsity as illustrated in Figure.1 (a), unlike the nature scene is various for interesting objects and modality, or the histopathological objects are sizable and clustered. To train with the plentiful data, on the one hand, the image augmentation on color and shape transformations or results of GAN is significant on the variant cervical dataset (Tan *et al.* (2021); Yu *et al.* (2021)), which is also a known trick in natural tasks and valid to deal with WSIs are multi-cohort or multicenter. On the other hand, despite there is no related work of cervical prediction, the procedure, firstly training in the primary labeled data and then complementing labels manually checked from unlabeled data predicted by trained models, is firstly proposed by Bertram *et al.* (2019) to efficiently augment the pathological database at the patch-level. Noteworthy, this study hypothesized that the reproducibility of pathologist-defined labels should with caution based on the improvement of this study, 0.034 $F1$ -Scores, and the larger 0.186 $F1$ -Scores by their further work (Bertram *et al.* (2020)).

The most of above works aimed for the patch-level prediction is based on the ROIs pathologist preselected. However, they ignored and underestimated the automatic selection of ROIs from the entire WSI. Although the ROI identification system proposed by Gupta *et al.* (2020) only make a coarse prediction, their results at a rough WSI-level covered all content of cervical smears and achieved a great accuracy of tile classification on a 10 LCT WSIs dataset from PAP smears. Based on the property of histopathological WSI that objects are sizable and clustered, relative methods for the CAD are deeply developed at the WSI-level. The public CAMELYON datasets (Litjens *et al.* (2018)) consists of 1,399 annotated WSIs of lymph nodes to detect breast cancer also promoted the development. The grand challenge CAMELYON17 has 37 algorithms to predict at the WSI-level using 899 learnable WSIs, where the top performance from the GoogleNet was reproduced based on the multi-scale and color normalization (Liu *et al.* (2017)), which with relatively shadow architecture and relatively longer train-

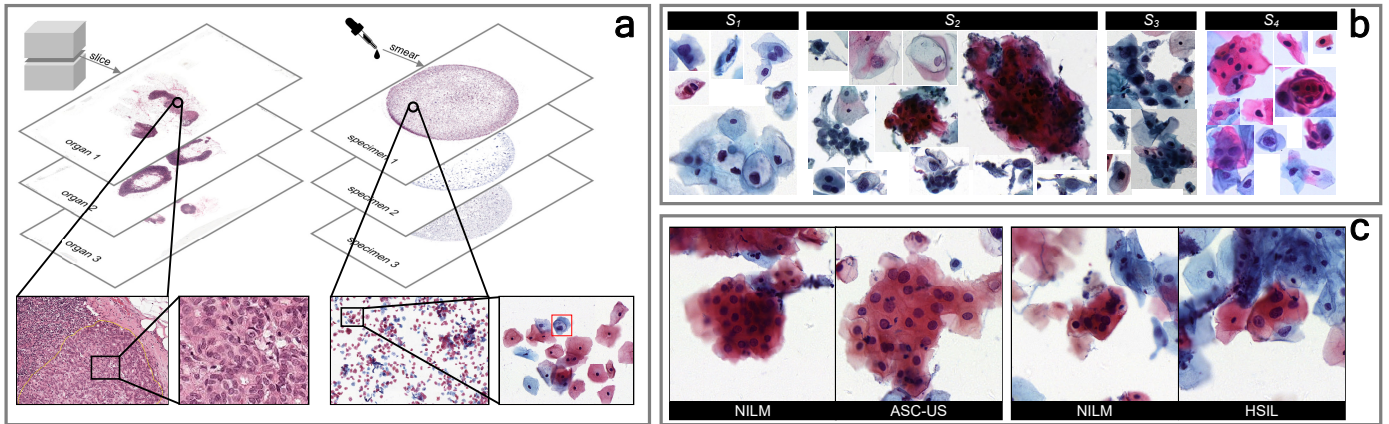


Fig. 1: The example of cytopathological WSIs used in this work, which illustrates three very challenging problems of the efficient analysis of LCT WSI from PAP smears. (a) The disparity between the histopathology and the cytopathology from CAMELYON dataset and our dataset, respectively, where the lesion area is highlighted with yellow line and red box. (b) The various properties and morphologies of the Atypical Squamous Cell (ASC), where S denotes different scanners, and (c) the analogous cells between normal and abnormal, which are named as Negative for Intraepithelial Lesion or Malignancy (NILM), ASC – undetermined significance (ASC-US) and High-grade Squamous Intraepithelial Lesion (HSIL).

ing phase than others. After the patch-level computation with CNN, this top method used the conventional machine learning and feature engineering to classify WSIs, which was surpassed by PFA-ScanNet that using more scales to extract features (Zhao *et al.* (2019)), then it was surpassed by the novel attention-based classifier with a shadower siamese MI-FCN architecture (Yao *et al.* (2020)). For the limited learnable data at the patch-level, weakly supervised learning is earlier employed for histopathological WSI-level prediction by Campanella *et al.* (2019), authors developed the multiple instance learning (MIL)-based method on the clinical application and achieved the better performance than pathologists with a huge 44,732 WSIs dataset.

For cytopathological WSI-level prediction, to deal with thyroid WSI, Dov *et al.* (2021) proposed the modified MIL approach that the instance selection is based on maximum likelihood estimation (MLE) with additional 4,494 labeled instances achieved 0.985 of AUC on a 908 WSIs dataset. DP-Net proposed by Lin *et al.* (2021) is claimed as the first deep learning-based method for the cervical WSI analysis from PAP smear. Their novel approach is a handcrafted logical classification strategy for the confusion of subclasses by automatically clustering abnormal cells in the middle hierarchy between classes, and achieved the best performance on their 19,303 cervical WSIs dataset with 560,536 patch-level annotations for the training phase. Zhu *et al.* (2021) proposed an integrated system that includes 24 target detection CNNs, one patch-based classification CNN and one nucleus segmentation CNN to compute cervical LCT smears, and one XGBoost and one logic decision tree to classify at the WSI-level. They create a new 24 classes to deal with confusing subclasses for each patch-level CNN and shown an appealing result on their 81,727 smears dataset. Cheng *et al.* (2021) proposed a robust WSI analysis for cervical cancer screening using deep learning. It is a progressive recognition method for the generalization problems of multicenter multiscanner data. They combined the low and high-resolution WSIs by two CNNs for the patch-level classifi-

cation, respectively, and enriched the augmentation of various train data. The WSI-level probabilities are computed by another recurrent neural network (RNN) based on the semantic feature from the high-resolution CNN. Their proposal achieved an appealing performance on their 3,545 WSIs based on 79,218 patch-level annotations.

The currently automatic cervical WSI analysis works, however, are not only based on the massive cost of the patch-level annotations but the WSI-level classification is not implemented by the affluent informational features. They generally established with a large number of manual annotations and gathered the patch classification probabilities or the single semantic features by a single classification task to represent the WSI. In this work, WSIs of our dataset are represented as the semantic and location features by dual tasks, that is classification task + location task (a.k.a. object detection).

In summary, there are three challenging problems of the efficient analysis of LCT WSI from PAP smears:

- i) For the overall WSI analysis, as illustrated in Figure.1 (a), the physical properties of cytopathology are different with histopathology. The former lesion zones are relatively few and small, while the latter is ubiquitous and sizable in lesion zones. Frameworks used in histopathology would be disadvantageous if disregarding such sparsity and subtlety of valuable objects in cytopathology WSIs.
- ii) Unlike natural tasks, pixels of pathology image are huge but the variety of texture is relatively limited. Although it was proved that deeper model can lead more performance by extracting the deep feature, cervical data needs more efficiency than depth of the model to complete the WSI-level task. As well as the discrepancy between abnormal and hard normal cells is slight, which causes the local lesion detection is highly dependent on the experience of cytopathologists. Several examples are shown in Figure.1 (b) and (c).
- iii) Traditional frameworks for WSI-level task adopted the overlap sampling method that repeatedly computes image

tile to reduce the severe cell truncation, which is a side effect that cells located in the edge of image could be cut. The performance will be thus reduced when meeting truncated cells. The redundant computation of overlap pixels, however, further drops the efficiency of WSI-level task.

The challenges and the problems mentioned above of the cytopathological tasks pose the specific design of CNN in this work. Firstly, feature representation and feature variety are the main factors of the CNN encoder are considered. Secondly, the model that able to provide the summary and brief feature should be lightweight, for workload reduction. Thirdly, the performance of the WSI-level classification should be not only great for WSIs from a single source but stable for different scanners and cohorts.

1.3. Our contributions

The shape annotation experts draw to bound the abnormal cells at the patch-level is credibly reproducible caused by non-cytopathological experiences. While the cytopathological experiences on the cervical content are dissimilar between different experts. Such noise of annotations can affect the performance of CNN, the feature representation for instance, especially for multi-cohort or multiscanner WSIs. The natural detection network includes feature maps fused the local size information and the object content into a single model that accomplishes dual tasks of lesion locating and content classifying, such as YOLO series (Redmon and Farhadi (2017, 2018)). Their potentiality to extract semantic and size features inspires us. We design an efficient cervical WSI analysis framework based on multi-scale semantic and location features using deep learning, and contributions are three points as follows corresponding the challenges:

- i) For the challenge i), we choose to design a detection model named YOLCO (You Only Look Cytology Once) to build our framework. Its feature mixes semantic and location information. Simultaneously, the feature is directly extracted inside the single cell/cluster instead of the traditional way that from image tile with a fixed size. According to this, we can avoid the cervical feature remaining at the fixed tile and the only semantic level.
- ii) For the challenge ii), we choose to enhance the performance of lightweight network. We proposed an inline connection network (InCNet) to replace normal convolution network. It has several groupwise connection inside one layer, and constructed by the efficient depthwise separable (DS) convolution. The proposal can improve the performance of lightweight model without increasing depths and parameters for cervical data.
- iii) For the challenge iii), we choose to extremely increase the size of input tile in our framework. Since the proposed YOLCO has the lightest weight, we can increase one side length of image tile from 10^2 to 10^4 level pixels, which can be directly adopted into our framework. With such megapixel input, the proposed method can compute one WSI in only 43 repeats, averagely, and it needs no overlap sampling cause that above side effect is weak in the small number of input.

Table 1: Nine cohorts of WSIs from the lab of the hospital² by four different scanners are used in this work, where $N_{ann.}$ denotes the number of bounding box annotations, *neg.* and *pos.* denote the normal slides and the abnormal slides, respectively.

| scanner | cohort | res _{sum} /pixel | slides | pos. | neg. | $N_{ann.}$ |
|---------|---|---------------------------|--------|------|-------|------------|
| S_1 | 1 st | 0.24 (20×) | 208 | 103 | 105 | 16,914 |
| S_2 | 2 nd | 0.24 (20×) | 537 | 160 | 377 | 3,060 |
| | 3 rd | | 221 | 120 | 101 | 0 |
| S_3 | 3 rd , 5 th | 0.18 (40×) | 166 | 166 | 0 | 0 |
| | 6 th , 7 th , 8 th | | 512 | 194 | 308 | 0 |
| | 9 th | | 66 | 66 | 0 | 0 |
| S_4 | 3 rd , 4 th , 5 th | 0.29 (20×) | 319 | 124 | 195 | 0 |
| Total | | | 2,019 | 933 | 1,086 | 19,974 |

2. Materials

As shown in the table 1, nine cohorts of WSIs from the lab of the hospital² are used in this work by four different scanners: S_1 - the version 1 of 3DHisTech Ltd., S_2 - the version 2 of 3DHisTech Ltd., S_3 - Shenzhen Shengqiang Technology Ltd., S_4 - Wuhan National Laboratory for Optoelectronics-Huazhong University of Science and Technology. Each device is set with a different parameter for scanning. All WSIs are sampled under 20× magnification with a subtle change of resolution except S_3 under 40×. Version 1 and version 2 of 3DHisTech Ltd. are different in slide preparation and staining scheme. Furthermore, each WSI includes average 4.5 billion pixels at the central circular foreground using OTSU method (Otsu (1979)).

Total 19,974 typical lesion areas annotated of 138 WSIs from the 1st and 2nd cohorts which overall positive cervical cells, atypical squamous cells of undetermined significance (ASC-US), low-grade squamous intraepithelial lesion (LSIL), atypical squamous cells cannot exclude HSIL (ASC-H), high-grade squamous intraepithelial lesion (HSIL), and squamous cell carcinoma (SCC), are grouped by experts in one foreground class in this work. For WSI-level annotations, the 8th cohort has manually labeled with an overall subclass by experts, and there are 39 ASC-US, 27 LSIL, 25 HSIL. While others have only binary annotations.

3. Method

This work proposes the simplistic pipeline of the efficient cervical WSI analysis via computing much bigger ROI in few repeats of the single model with rethought of the connection approach in CNN. Increasing the input size from 10^2 to 10^4 is credibly to decrease the side effect, that is the truncated cells when cropping small images, and the additional processing, since WSIs are normally 10^4 pixel level of one side in our datasets.

For merging the mixed features in the cytopathological WSI computation and recognizing the cervical cells, the design is described in this section. Furthermore, the complex feature of cytopathology is enhanced by the novel InCNet as well as its principle and interpretation are depicted.

²The Maternal and Child Hospital of Hubei Province

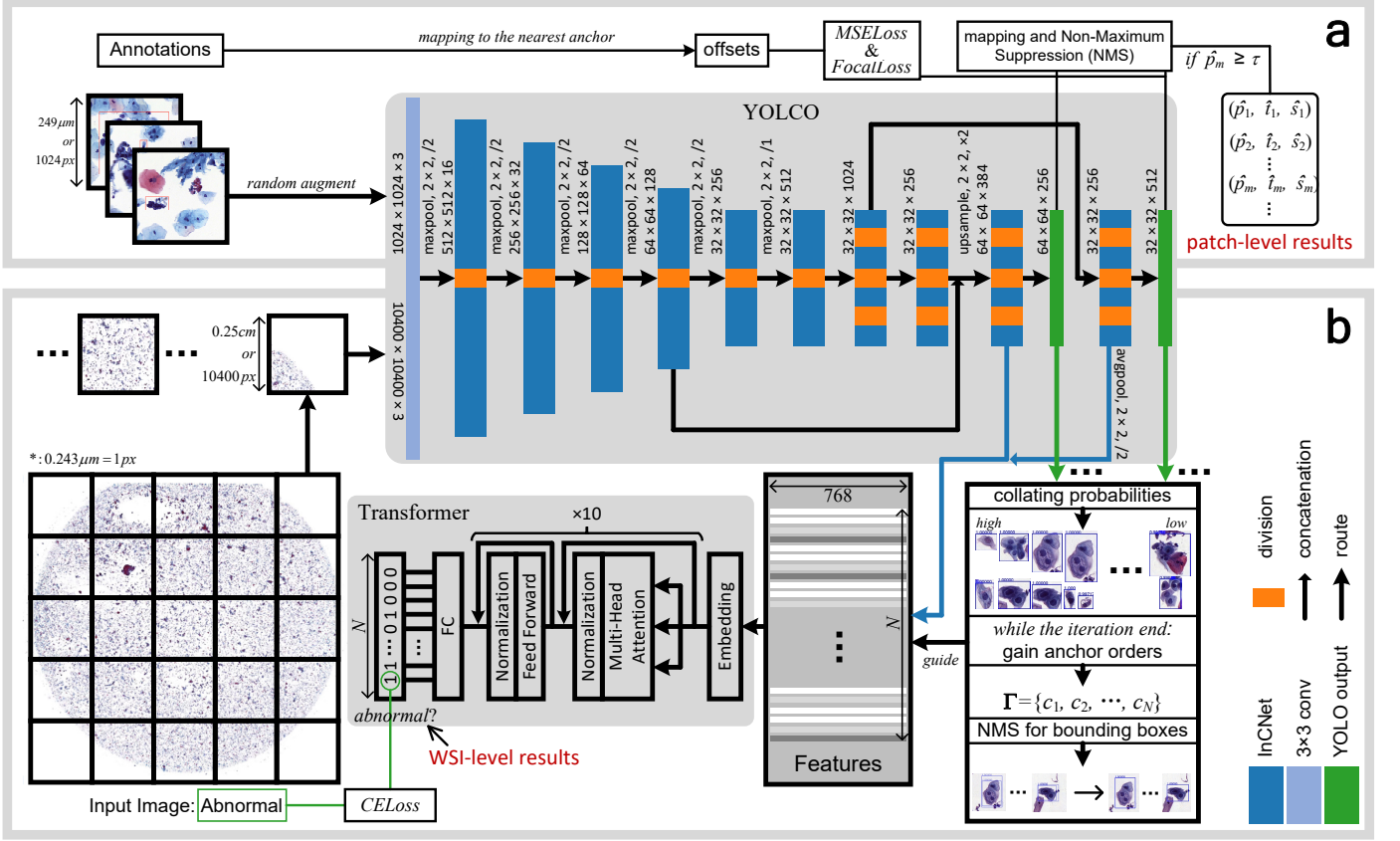


Fig. 2: The pipeline of the proposed method. (a) The process for cervical lesion detection at the patch-level in preselected ROIs. (b) The process for the automatic cervical diagnosis for the normal/abnormal classification at the WSI-level with top- N lesion area.

3.1. Framework

To start with, briefly describing the pipeline of our method to analyze WSIs that consists of two main parts. As shown in Figure.2 (a), firstly, training the lightweight model YOLCO at the patch-level, which has the same structure of the tiny-YOLOv3 (Tiny) and is built by lighter InCNet modules with the depthwise separable (DS) convolution, to attain the WSI encoder and the abnormal cells detector at the same time. The function that enhances the cervical representation provided by InCNet (see Section.3.2) is plugged throughout the model except for the input layer and the output layer of each scale level. LeakyRELU is the activation for each layer except the output layer. YOLCO consists of two levels of the scale with 2^5 the downsample ratio at 9^{th} conv-layer or 2^4 the downsample ratio at 10^{th} conv-layer in two branches, respectively. Another part, Figure.2 (b), is the efficient diagnosis achieved via the property of YOLCO of changeable input size and super lightweight to strikingly reduce the repeated computations, based on the same magnitude of each side between stitched patches and the central foreground in the WSI. YOLCO improves the speed of encoding and recognizes the WSI as the common detection task. The sequence of features mixed at two levels of the scale from the input of every output layer is collected via top- N probabilities guided of the corresponding non-repetitive coordinate of the anchor before the non-maximum suppression (NMS), which would expel neighboring feature vectors that cooperatively represent com-

plex objects. The WSI-level classification is completed with an additional sequence classifier, Transformer (Vaswani et al. (2017)) or simpler traditional methods (see Section.5.3.2), for the WSI feature embedding.

For the details of training YOLCO, the patch-level labeled data is randomly cropped as 1024×1024 RGB images enable to embrace every bounding box in our datasets. Assuming M annotations for cervical lesion is denoted by $\mathbf{T} = \{\mathbf{t}_m\}$, $\mathbf{t}_m \in \mathbb{R}^2$ the center point of lesion area, $\mathbf{S} = \{\mathbf{s}_m\}$, $\mathbf{s}_m \in \mathbb{R}^2$ the size of lesion area and $\mathbf{P} = \{p_m\}$, $p_m \in \{0, 1\}$ the target label for determining positive or negative. For the prediction and WSI representation at the patch-level, anchors are the common ingredients to train the detection CNN, which transmute the problems from solving Euclidean coordinates and sizes of boxes to estimating offsets of the nearest anchor denoted $\mathbf{G} = \{\mathbf{g}_c\}$, $\mathbf{G} \in \mathbb{N}^{2 \times C(l)}$ the coordinate of grid points, where $C(l) = w(l) \times h(l)$ the width times the height of the l^{th} layer, and $\mathbf{A} = \{\mathbf{a}_i\}$, $\mathbf{A} \in \mathbb{R}^{2 \times n_a}$ the size of the anchor with n_a the number of shapes. Three sizes of the anchor are set via the k -means clustering with $k = 3$ in this work. Then the annotation is mapped as $\mathbf{B} = \{\mathbf{q}_m, \mathbf{v}_m\}$, $\mathbf{B} \in \mathbb{R}^{(2+2) \times M}$ the offset of anchors to supervise the prediction of YOLCO, where

$$\begin{aligned} \mathbf{q}_m &= \arg \min_{\mathbf{t}_m - \mathbf{g}_c} \|\mathbf{t}_m - \mathbf{G}\|^2, \\ \mathbf{v}_m &= \arg \max_{\log(s_m/\mathbf{a}_i)} iou_s(\mathbf{s}_m, \mathbf{A}), \end{aligned} \quad (1)$$

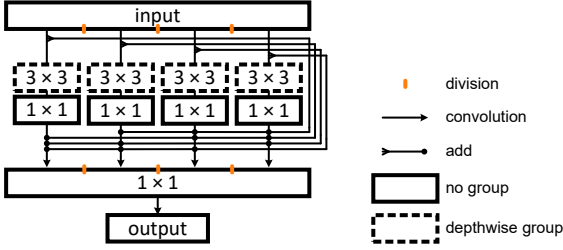


Fig. 3: The proposed convolutional inline connection network (InCNet) with 3 times of division for example.

and iou_s is the ratio of the inter area to the union area between two shapes of the box with the same coordinate. The order of the nearest anchors, $\mathbf{O} = \{\mathbf{o}_m\} = \{\arg \min_c \|\mathbf{t}_m - \mathbf{G}\|^2, \arg \min_i iou_s(\mathbf{s}_m, \mathbf{A})\}$, $\mathbf{O} \in \mathbb{N}^{2 \times K}$, is collected in the meantime.

Consequently, the output of YOLCO is fitted as the offset of every anchors that named as $\mathbf{Y}^{box} = \{\hat{\mathbf{q}}_{c,i}, \hat{\mathbf{v}}_{c,i}\}$, $\mathbf{Y}^{box} \in \mathbb{R}^{(2+2) \times C(l) \times n_a}$ and $\mathbf{Y}^{cls} = \{\hat{p}_{c,i}\}$, $\mathbf{Y}^{cls} \in \mathbb{R}^{C(l) \times n_a}$, for each anchor of each grip point in the feature map, then we employ the mixed loss function as follow:

$$\mathcal{L}_{total} = \mathcal{L}_{box}(\mathbf{B}, \mathbf{Y}_{obj}^{box}) + \alpha \cdot \mathcal{L}_{cls}(\mathbf{P}, \mathbf{Y}_{obj}^{cls}) + \beta \cdot \mathcal{L}_{cls}(\mathbf{P}, \mathbf{Y}_{noobj}^{cls}), \quad (2)$$

where $\mathbf{Y}_{obj}^o = \{\mathbf{Y}^o | \{c, i\} \in \mathbf{O}\}$, $\mathbf{Y}_{noobj}^o = \{\mathbf{Y}^o | \{c, i\} \notin \mathbf{O}\}$, and $\alpha = 1, \beta = 100$ control the balance between the coordinates and sizes of object and the classification of foreground and background.

$$\begin{aligned} \mathcal{L}_{box} &= MSE_{Loss}(\mathbf{B}, \mathbf{Y}^{box}) \\ &= \frac{1}{K} \sum_k (\|\mathbf{q}_m - \hat{\mathbf{q}}_m\|^2 + \|\mathbf{v}_m - \hat{\mathbf{v}}_m\|^2), \end{aligned} \quad (3)$$

$$\begin{aligned} \mathcal{L}_{cls} &= Focal_{Loss}(\mathbf{P}, \mathbf{Y}^{cls}) \\ &= -\frac{\theta}{K} \sum_k (1 - \hat{p}_m)^\gamma p_m \log(\hat{p}_m + \epsilon) \\ &\quad - \frac{1 - \theta}{K} \sum_k (\hat{p}_m)^\gamma (1 - p_m) \log(1 - \hat{p}_m + \epsilon), \end{aligned} \quad (4)$$

where $\theta = 0.95, \gamma = 1, \epsilon = 1e-9$ are parameters of the focal loss with default settings (Lin *et al.* (2017)). Naturally, the predicted offset of anchors will be gathered by τ the probability threshold in the patch-level test phase without \mathbf{O} , then $\{\hat{\mathbf{T}}, \hat{\mathbf{S}}, \hat{\mathbf{P}}\} = \{\hat{\mathbf{q}}_{c,i} + \mathbf{g}_c, \exp(\hat{\mathbf{v}}_{c,i}) \cdot \mathbf{a}_i, \hat{p}_{c,i} | \hat{p}_{c,i} \geq \tau\}$ the predicted boxes by inversely operated from the Equation.1 are transported to NMS for the patch-level results.

For the details of the WSI-level analysis as shown in Figure.2 (b), the RGB WSI is split with size of 10400×10400 as the same magnification as the patch-level from the center to the peripheral of the circle of the smear using OTSU (Otsu (1979)) at scale-level 8, where scale-level means the image is down-sampled x times using $ratio = 2$ each time ($x = 8$ in this case). Comparing with the patch-level, the threshold is set as $\tau = 0$ for top- N collecting by the order $\mathbf{\Gamma} = \arg \text{sort}_c \hat{\mathbf{P}}$, $\mathbf{\Gamma} \in \mathbb{N}^{2 \times C(l) \times n_a}$, where the collecting approach is considered with the spatial

restriction (see Section.4.1.2). Then mapping $\mathbf{X}, \mathbf{X} \in \mathbb{R}^{768 \times N}$ the set of lesion area feature embeddings in a given WSI to $\mathbb{R}^{D_{FF} \times N}$ as $\hat{\mathbf{X}}$ by Transformer with D_{FF} the dimension of Feed Forward layer. Finally, the WSI-level results are attained via NMS($\hat{\mathbf{T}}, \hat{\mathbf{S}}, \hat{\mathbf{P}}$) to detect abnormal cells, and the last prediction of $\text{sigmoid}(\mathbf{W}_{mlp} \hat{\mathbf{X}})$, with the parameter of the last full connection (FC) layer, $\mathbf{W}_{mlp} \in \mathbb{R}^{n_{cls} \times D_{FF}}$, is supervised by the cross entropy loss (CE_{Loss}), where the number of class $n_{cls} = 2$.

3.2. Inline Connection Network (InCNet)

Since the complexity of cervical objects varies, it is left to task heads, FC layer, or the pointwise convolution layer of natural CNNs whether the multistep (Ren *et al.* (2015)) or the single step (Redmon and Farhadi (2018)), which are burdened with additional problems in this special scene while the task supervision is the most attentive.

As shown in Figure.3, the InCNet is inspired by the group convolution and has a similar motivation with the inner skip connection (Res2Net by Gao *et al.* (2021)). It poses the multiple groupwise connections inner the module to enrich the connectivity between 3×3 filters and 1×1 filters with a lighter structure, which is based on the concept that the DS convolution acts the same function of the normal convolution (Howard *et al.* (2017)). The receptive field (RF) for the cervical cell image hardly encodes all information with the single size filter, since the local pattern of the sparse lesion is more important and complex than the dense region that covers the normal cell or the background. The groupwise connection between them guides multi-scale RFs and enhances the performance of the local pattern. Especially, the connection attaches the output of 3×3 filters for a bigger RF and 1×1 filters for a smaller RF of l^{th} layer as the same level of nonlinearity:

$$\mathbf{x}_{l+1} = \text{LeakyReLU}(\mathcal{P}(\{\mathcal{D}(\mathbf{x}_l[l]) + \sum_{j \neq l} \mathbf{x}_l[j]\}_{l=1 \sim n_g})) \quad (5)$$

where \mathcal{P}, \mathcal{D} are the pointwise convolution and the DS convolution, respectively, $x_l[l]$ is the l^{th} group of the input of l^{th} layer with n_g is the count of group with $n_g - 1$ times of even division in the channel direction.

Moreover, the skip connection is non-considered for the efficiency of the proposed model caused that the shallow CNN is viable to propagate gradients of each node even the deepest node without the residual learning (He *et al.* (2016)).

4. Train and Inference

As mentioned in the method section, for the WSI classification, models of the proposed framework need first to train at patch-level, and then to compute WSIs. The final WSI classification result is depends on the representation of cells at patch-level. Meanwhile, the abnormal cell detection performance can show which areas lead the final result. Thus, in this section, we describe the procedure of train and inference of every model compared in our experiments, and the train-val-test data setting at both patch-level and WSI-level.

Table 2: The implement and properties of CNN encoders in experiments, where N_c is the total length of the feature sequence from η scales, or the single scale with $\eta = 1$, N_{tile} the average number of input tiles from WSI, CE the cross entropy loss, and MACs the Memory Access Costs, which means multi-add calculation, calculated by the python tool, thop.

| | Input side length (px) | | Params(M) | MACs(G) <small>$1024 \times 1024 \times 3$</small> | Loss func. | Data augments | N_{tile} | $N_c, \langle \eta \rangle$ |
|-------------------|----------------------------|-----------|---------------|--|--------------|---------------------------|------------|-----------------------------|
| | Patch-level | WSI-level | | | | | | |
| MNV2 | 320 | 8320 | 2.23 | 6.54 | CE | shift, normalize | 68 | 1280, $\langle 1 \rangle$ |
| InCNet $_{n_g=8}$ | | 6944 | 2.79 | 10.08 | | | | |
| AFR | 1024 | 2080 | 41.98 | 148.85 | MAE, CE | flip, rotate, scale, blur | 1276 | - |
| YOLOv3 | 1024 | 2080 | 61.52 | 198.47 | $MSE, Focal$ | shift, scale | 1276 | 1792, $\langle 3 \rangle$ |
| Tiny | | | 8.67 | 16.60 | $MSE, Focal$ | | | |
| YOCO | 1024 | 10400 | 1.79 | 3.55 | $Focal$ | shift, scale | 43 | 768, $\langle 2 \rangle$ |
| YOLCO | | | 1.79 | 3.55 | $MSE, Focal$ | | | |

4.1. Models in experiments

Total 7 CNNs as shown in Table.2 are trained with annotated bounding boxes among 1st and 2nd cohorts in our experiments. The first consideration for choosing compared models is the framework:

- The related work for WSI analysis by Cao et al. (2021) consists of a detector, AttFPN-Faster-RCNN (called AFR), and a patch image classifier, ResNet50. Its framework is similar with the proposal and has three steps of WSI inference: (i) detecting bounding boxes, (ii) classifying the input image of detector by the detected top-4 boxes, and (iii) predicting the WSI classification using the mean probability of top-10 images. Thus, we use the same setting as our framework to train AFR + ResNet50.
- The proposed framework has two steps of inference: (i) detecting bounding boxes that separately correspond to one feature vector, (ii) classifying the collection of feature vectors of top- N boxes as the WSI-level class. The proposed YOLCO is the detector in this framework. It is based on the version 3 of YOLO by Redmon and Farhadi (2018) (called YOLOv3) and its Tiny version (called Tiny). YOLOv3 and YOLCO have same structure but different backbone. The difference between Tiny and YOLCO is only the replacement of normal convolutional layers by InCNet layers using the same channel number of input and output, and they have more balanced parameters.
- To generate feature vector, traditional CNN encoder is supervised by the classification task instead of detecting bounding box. Therefore, we test an imperfect version of the proposed framework by using classifier to replace the detector, including the state-of-the-art (SOTA) MobileNetV2 by Sandler et al. (2018) (called MNV2), InCNet $_{n_g=8}$, and YOCO. The difference between MNV2 and InCNet $_{n_g=8}$ is only the replacement of normal DS layers by InCNet layers using the same channel number of input and output. YOCO is the strict contrast version, which has the same architecture and training process as YOLCO but the removal of the box representation (\mathcal{L}_{box}), to display the significance of dual tasks.

Aside from the previous work AFR that is strictly tested as same as the public code, according to the weight and the supervision of CNNs, different setting of O and train-val-test procedure are used in our framework, respectively.

First, the overlap of input image sampling in the inference is set as $O = 0$ for the lightweight CNNs because the input size can be extremely increased, including MNV2, InCNet $_{n_g=8}$, YOCO, and YOLCO, while YOLOv3 is set as $O = 288$. For $O \neq 0$, the post-processing, which stitches feature maps in the overlap area, is a max sampling approach with the probability maximum.

Second, the data augmentation in Table.2 is randomly applied in the training phase of both detectors and classifiers with $p = 0.5$. There are 200 epochs at most of the learning at patch-level.

For training detectors, the input image is size of 1024×1024 pixels, and output feature vectors is size of $32 \times 32 \times N_{ch}$ with the channel number N_{ch} . While the input is 320×320 for training classifiers, like MNV2, and the output is $1 \times 1 \times N_{ch}$.

Thus, for the inference, except for YOCO and other detectors that output feature vectors corresponding the area is size of 32×32 pixels, feature vectors of MNV2 and InCNet $_{n_g=8}$ are 320×320 . The enlarged input size at WSI-level of inference as listed in Table.2 is set based on the storage capacity of the GPU.

Finally, feature sequence classifiers, e.g. Transformers, are all learning for 300 epochs. All trains have the same learning schedule and beginning at $lr = 0.000005$.

Furthermore, all the classification experiments at both patch- and WSI-level consist of six loops of train-val-test because of limited number of our slides.

4.1.1. Sequence classifiers in our framework

For certifying the ability of feature representation of the proposed method, four types of classifiers are discussed:

(i) SVM, the conventional machine learning method using the default setting implemented by the scikit-learn toolbox, (ii) RNN, the recurrent neural network using one recurrent layer and 2048 features in the hidden state and being implemented by PyTorch,

(iii) LSTM, the recurrent neural network with memory function as the same parameters setting with RNN,

Table 3: Two Settings of train, validation and test in the classification task. Set 1 is divided by the scanner, and Set 2 is divided by if data is seen/unseen/mixed for model.

| Group | <i>pos. slides</i> | | | <i>neg. slides</i> | | |
|--------------|--------------------|-----|------|--------------------|-----|------|
| | train | val | test | train | val | test |
| Set 1 | | | | | | |
| S_1 | 88 | 7 | 8 | 90 | 8 | 7 |
| S_2 | 242 | 18 | 20 | 412 | 34 | 32 |
| S_3 | 371 | 26 | 29 | 270 | 20 | 18 |
| S_4 | 109 | 8 | 7 | 171 | 12 | 12 |
| Set 2 | | | | | | |
| seen | 225 | 18 | 20 | 414 | 35 | 33 |
| unseen | 585 | 41 | 44 | 529 | 39 | 36 |
| mixed | 810 | 59 | 64 | 943 | 74 | 69 |

(iv) Transformer³, the neural network solely based on attention mechanisms using the recommended parameters setting that repeats Transformer layer 10 times and the number of hidden features is 2048.

Except for SVM, all classifiers are training with a dropout layer with a 0.5 drop rate, considering the avoid overfitting for their FC layers. Note that the sorting order of the count of parameters is (iv)>(iii)>(ii), and (i) is directly computing the hyperplane of all vectors of the input sequence flatten into one column without additional parameters.

4.1.2. WSI-level feature Collecting in our framework

The collection of cervical feature extraction is the smallest step but not least. The reason is that the feature vector from detectors is corresponding to a smaller area (in our case, 32×32) than the classifiers (e.g. 320×320 in MNV2). Therefore, since the size of abnormal cell is larger than the computing area, the number of vectors will be various if there is no limitation of collection. Two collecting methods are designed to assess:

(i) The normal one is a Euclidean distance threshold D to restrict feature vectors of top- N boxes, where $N \leq 500$ considering that the long sequence classification is challenging. The collecting area with lower score will be reject if the distance between two areas is smaller than D .

(ii) B_{box} is the other one that guided by the predicted bounding box of the lesion area via collecting 10 feature vectors inside each top- N boxes, which means $10 \times N$ vectors will be gathered.

4.2. Data Setting

4.2.1. Private data

The private 2,019 slides dataset consists of nine cohorts since there are different individuals produced in different circumstances. The local annotations at the patch-level are derived from WSIs among 1st and 2nd cohorts as shown in Table.1 with a limited amount. For the final WSI classification, all 2,019 slides are split to test the performance.

Slide data in our experiments are averagely split for train, validation and test of deep learning models with 85%:7.5%:7.5%,

as listed in Table.3. Because our final goal is WSI classification, there is no test set for CNN detectors/classifiers but only validation set (15% of the whole data) to choose the best model. Train, validation and test data of classification tasks are set in 2 ways as listed in Table.3.

In addition to the diagnosis label of each group is slightly uneven caused by the habit of individual experts, the cervical content of WSI varies with the unique parameter setting of 4 different scanners mentioned in Section 2. The division by different scanners is "Set 1" hence.

Besides, the discrepancy between nine cohorts is considered to perform the cervical feature representation of CNN detectors learned from the seen data, that is the local annotation among 1st and 2nd cohorts. Otherwise, the unseen data consists of other cohorts has never been learned for local recognition. It is more challenging for the generalization of CNNs. The division by seen/unseen/mixed is "Set 2" hence.

Each annotation is used once in each training epoch in every task. For training detectors, the bounding box is restricted inside the input image. It is the same for training classifiers, and the input image will be restricted inside the bounding box if the box size is larger than the image.

4.2.2. Public data

A public dataset by Plissiti et al. (2018) is used in our experiments to further show the significance of the proposed CNN. This dataset is divided into five classes and consists of total 4,049 cell images.

Following their experiments for patch-level classification task, we process a 5 cross-validation and run the best model (VGG19) for the comparison. Except for the input size is 80×80 as the same as the literature, other details of training like learning rate are the same as our CNN classifiers.

5. Experimental Results

There are two types of experimental results to illustrate the efficiency and the significance of the proposed method:

- (1) The WSI classification for cervical diagnosis.
- (2) The patch detection/classification for the lesion area.

5.1. Evaluation metrics

The common estimation methods are used for the assessment. The true positive (TP), false positive (FP), true negative (TN), and false negative (FN) are the basic evaluation of results, thus the computations are as follows.

- (1) Accuracy (Acc.), Sensitivity (Sens.), Specificity (Spec.), and the Receiver Operating Characteristic Curve (ROC) for classification tasks, as well as the nonparametric bootstrapping with 1,000 samples, was used to compute 95% confidence intervals.

$$\begin{aligned}
 \text{Acc.} &= \frac{TP}{2(TP + FP)} + \frac{TN}{2(TN + FN)}, \\
 \text{Sens.} &= \frac{TP}{TP + FN}, \\
 \text{Spec.} &= \frac{TN}{TN + FP}.
 \end{aligned} \tag{6}$$

³Transformer codes are from <https://github.com/lucidrains/vit-pytorch>

- (2) Precision (Prec.), Recall (Rec.), and mean of average precision in the precision-recall curve (mAP) for detection tasks.

$$\text{Prec.} = \frac{TP}{TP + FP}, \text{Rec.} = \frac{TP}{TP + FN}. \quad (7)$$

5.2. Implement details

The whole experiment is implemented by PyTorch based on Windows 10 OS with one Xeon(R) 6134 CPU@3.20GHz and one Tesla P40 GPU. All models are training with the Adam optimizer and the Cosine learning rate reduction schedule. Aside from the code of ARF is obtained from github, other models are implemented by torchvision package.

5.3. Quantitative results at WSI-level

Experiences in Set 1 show the performance of methods for different scanning devices. As shown in Table.4, the proposed YOLCO has the highest average accuracy (AVG), 86.2%, and the lower fluctuation of all data groups. It precedes the second-best YOLOv3 with 6.4% higher accuracy as well as the robustness with 0.009 lower STD (standard deviance) and 0.095 lower MD (max difference). Despite the subtle lower STD of Tiny and MNV2, and lower MD of Tiny than YOLCO, the much lower accuracy is unacceptable to diagnose cervical slides, which is mainly affected by that it has just surpassed 60% accuracy in scanner S_2 of Tiny or in scanner S_4 of MNV2. A similar hardship occurs to YOLOv3 in that the performance in S_2 is unmatched with remains. YOLCO is considerably stable and efficient than common models, with the maximum accuracy in S_4 and more powerful in the above hardship, based on the feature representation enhanced by InCNet.

As shown in Table.5, we get the generalization of each method when it is test on unseen or mixed data in Set 2. YOLCO with 79.7% average accuracy has the highest precision than others but the most susceptible whether on seen/unseen/mixed data with the highest MD 0.242. It is reasonable that the deep learning network has the best capability for seen cervical slides, has the worst for unseen cervical slides, and the mixed data is in the middle. The existent pattern of this statement is suspicious of YOLOv3 with the similar accuracy of unseen and mixed data, and it shows the norm of the ability of YOLCO that it is limited when feature extraction is learned from relatively few amount of annotations and few amount of parameters.

As for the further revealing, the ROC curve as shown in the top of Figure.4 (a) from the last run of loops in our mixed data denotes not only classification accuracy but the probabilities provided by YOLCO are more accurate than the performance of common CNNs. The higher area under the curve (AUC) score also quantitatively shows our method more accurate than the best of others: 0.872 of YOLCO vs 0.867 of YOLOv3. And the box chart at the bottom displays the distribution of probabilities that our method performs better.

5.3.1. Performance on positive subclasses

Since the clinical concern is more lie on the high sensitivity of severe types, like HISL, we show such results on our 8th cohort slides in Table 6.

5.3.2. Ablation studies: sequence classifiers

Comparing with YOLOv3, Tiny, MNV2, and our method, different classifiers are adopted into our framework for 2,019 WSIs as shown in Table.7. And, Figure.4 (c) bottom is ROC results of our method in the last run of repeated experiments.

Our method, YOLCO, displays the best performance on every classifier except LSTM from 72.6% to 80.8%. In contrast, a striking gap between accuracies of the second, YOLOv3 from 58.5% to 80.6%, indicates its inferior feature representation. Furthermore, even though YOLOv3 has 78.7% accuracy based on a relatively more complex classifier, the proposed method is superior using the non-parametric SVM.

5.3.3. Ablation studies: collecting methods

As shown in Figure.4 (b), it is apparent that more features from cervical slides lead to better performance of feature representation, as well as the AUC score improved from 0.740 to 0.895 when N is increased from 10 to 200. It is fallen when more boxes are chosen, however, since the long sequence classification is a challenging task.

A glance at the bottom ROC figure reveals the features are valuable and rich between the neighboring patch that 0.93 the best AUC is achieved via $D = 0$. An another evidence is that $D = 2$ leads the worst results, where the edge of abnormal cells have more chance to be collected than the center cause of *size of nucleus* $< D <$ *size of cell*. The weak but not the worst method (ii) B_{box} hardly reaches a better performance.

5.3.4. Dual tasks: classification + location

To illustrate the significance of the proposed feature mixture, the WSI-level ablation study is executed by comparing between performances of CNNs producing single feature under the single supervision, the classification, or feature mixture under the dual task, classification + location.

In the Table.8, and the top of Figure.4 (c), given are performances of classification at patch-level with the equivalent number of negative patches, and performances at WSI-level, respectively. Reasonably, the AUC score has 0.034 up at the path level classification after the box loss deducting in YOCO but has 0.091 down that feature mixture is more valid at the WSI-level based on the proposed idea. And, InCNet _{$n_g=8$} achieves 0.964 a remarkable AUC at patch-level with 0.005 higher than the SOTA model and others, as well as the same cohorts at WSI-level with 0.89 AUC. But, it becomes 0.722 the lowest at the WSI-level as similar as remains without \mathcal{L}_{box} for all cohorts including unseen data.

5.4. Feature Representation Qualitative results

5.4.1. Feature variety

The feature variety is depicted via the visualization of the feature map of CNNs as shown in Figure.5, to illustrate the weakness of natural upstream CNNs and the advantage of the proposed YOLCO. The activated part in every feature map in the figure has a higher value than the non-activated value, which is less than or equals 0 based on the LeakyRELU function. And, both Tiny, YOLOv3, and YOLCO generate feature maps at multiple scales from the 1024×1024 RGB input image.

Table 4: Results per scanning type of WSIs: Classification performance using Transformer classifier in Set 1, where AFR is the method in Cao et al. (2021)

| | AFR | Tiny | | | MNV2 | | | YOLOv3 | | | YOLCO | | |
|----------------|-------|---------|---------|---------|---------|---------|---------|---------|---------|---------|--------------|---------|---------|
| | Acc. | Acc. | Sens. | Spec. | Acc. | Sens. | Spec. | Acc. | Sens. | Spec. | Acc. | Sens. | Spec. |
| All S | .603 | .65±.03 | .60±.13 | .70±.09 | .70±.02 | .66±.13 | .74±.12 | .78±.02 | .84±.04 | .71±.06 | .78±.03 | .86±.04 | .69±.08 |
| S ₁ | .652 | .74±.06 | .85±.13 | .62±.16 | .82±.06 | .73±.09 | .90±.07 | .84±.03 | .83±.06 | .86±.00 | .80±.04 | .80±.13 | .80±.07 |
| S ₂ | .672 | .62±.01 | .51±.12 | .73±.11 | .70±.02 | .60±.10 | .80±.07 | .66±.02 | .66±.14 | .66±.10 | .90±.03 | .97±.04 | .83±.04 |
| S ₃ | .662 | .64±.03 | .53±.22 | .75±.24 | .71±.02 | .69±.11 | .73±.09 | .76±.01 | .74±.12 | .78±.13 | .82±.04 | .79±.09 | .86±.06 |
| S ₄ | .583 | .79±.02 | .74±.15 | .85±.12 | .60±.07 | .52±.30 | .68±.39 | .95±.03 | .94±.07 | .97±.04 | 1.0±.00 | 1.0±.00 | 1.0±.00 |
| AVG | 0.634 | 0.688 | | | 0.705 | | | 0.798 | | | 0.862 | | |
| STD | 0.035 | 0.074 | | | 0.080 | | | 0.098 | | | 0.089 | | |
| MD | 0.089 | 0.236 | | | 0.438 | | | 0.366 | | | 0.271 | | |

Table 5: Results on seen, unseen, and mixed WSIs: Classification performance using Transformer classifier in Set 2, where AFR is the method in Cao et al. (2021)

| | AFR | Tiny | | | MNV2 | | | YOLOv3 | | | YOLCO | | |
|--------|-------|---------|---------|---------|---------|---------|---------|---------|---------|---------|--------------|---------|---------|
| | Acc. | Acc. | Sens. | Spec. | Acc. | Sens. | Spec. | Acc. | Sens. | Spec. | Acc. | Sens. | Spec. |
| seen | .723 | .62±.01 | .42±.07 | .82±.08 | .82±.01 | .86±.03 | .77±.03 | .80±.02 | .79±.07 | .81±.06 | .89±.01 | .87±.05 | .90±.03 |
| unseen | .542 | .61±.02 | .78±.10 | .45±.13 | .66±.01 | .47±.14 | .86±.13 | .78±.01 | .71±.10 | .84±.09 | .72±.04 | .70±.22 | .73±.16 |
| mixed | .603 | .66±.02 | .65±.09 | .68±.08 | .70±.02 | .66±.13 | .74±.12 | .78±.02 | .84±.04 | .71±.06 | .78±.03 | .86±.04 | .69±.08 |
| AVG | 0.622 | 0.630 | | | 0.726 | | | 0.786 | | | 0.797 | | |
| STD | 0.075 | 0.027 | | | 0.067 | | | 0.021 | | | 0.075 | | |
| MD | 0.181 | 0.108 | | | 0.188 | | | 0.084 | | | 0.242 | | |

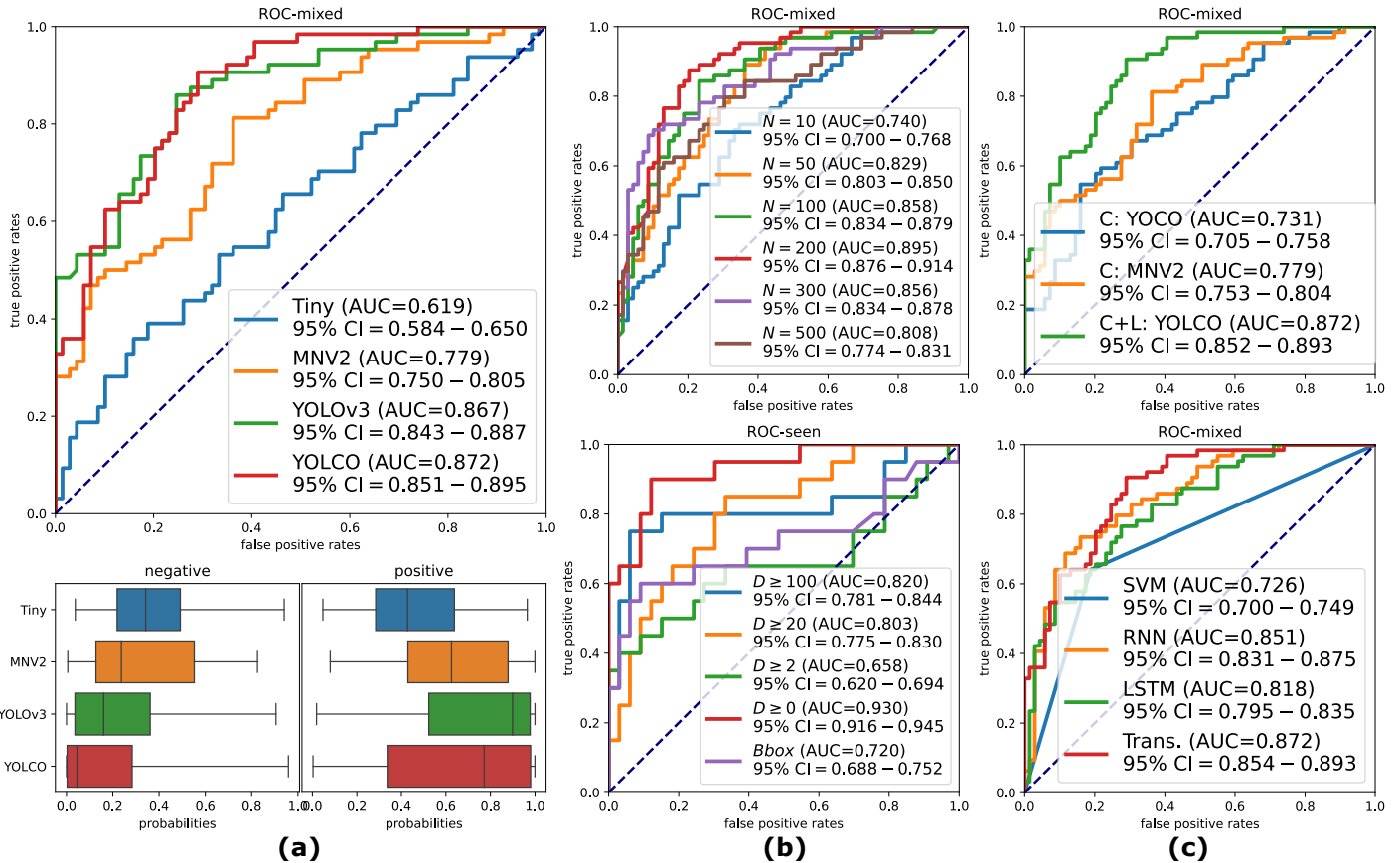


Fig. 4: The quantitative results of ROC curves and probabilities distribution, where the last run of loops for the sequence classification model is illustrated for each method, and 95% CI is the 95% confidence interval. (a) shows the overall performance on our 2,019 WSIs data using Transformer classifier; (b) shows the effect of parameters changing for the proposed method by controlled variables, where "Bbox" denote collecting method ii, N varies with $D = 0$, and D varies with $N = 100$; and (c) shows the WSI-level comparison between multiple tasks and the single task at the top, and the usage of different classifiers of our method at the bottom.

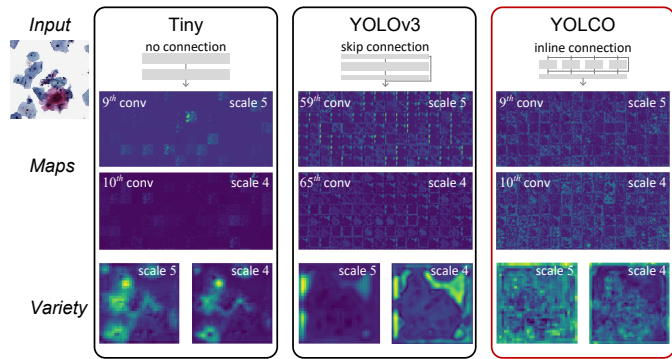
In the maps of the figure, with no connection, Tiny using the same build of convolutional modules as YOLCO has the fewest activated feature maps, which consist of more than half of nearly non-activated. With skip connection, YOLOv3 using the much deeper structure and bigger parameters can generate

much more feature maps (1792 channels). It performs an overwhelming similar pattern of activation but much better than its downgraded version, Tiny.

In the variety of the figure, the natural upstream CNNs, Tiny and YOLOv3, are both have a similar pattern of variety of their

Table 6: Performance of YOLCO (mixed) on positive subclasses of 8th cohort WSIs.

| | <i>neg.</i> $n = 144$ | ASC-US $n = 39$ | LSIL $n = 27$ | HSIL $n = 25$ |
|-------------|--------------------------|--------------------|------------------|------------------|
| Accuracy | 0.837 | 0.849 | 0.753 | 0.786 |
| Sensitivity | 0.933 | 0.867 | 1.000 | 1.000 |
| Specificity | 0.740 | 0.831 | 0.507 | 0.571 |

Fig. 5: The feature variety of the proposed model against two other conventional CNNs. All feature maps are extracted from the last layer before the output layer at each level of scale with the presented input image, where the downsampling ratio is 2^x with scale x . The variety is the channel-wise standard deviation of feature maps.

feature maps at two scales, while YOLCO has the most various feature maps. High values of upstream CNNs are existed but not in the most important abnormal cells on the lower and central parts of the input image. That is the weakness for subsequent WSI classification based on those features.

5.4.2. *t*-SNE

To illustrate the discrimination and the feature representation between CNNs, the WSI-level features are embedded into the 2D plane using the t-SNE toolbox (Van der Maaten and Hinton (2008)) with the same random seed (142857). SVM, LSTM, and Transformer results are point in the t-SNE results from the $n_c * N$ dimensional features for SVM from CNNs, and the features for LSTM and Transformer from the last hidden state, respectively.

As shown in Figure.6, it is clear to found that the S_2 data are the most challenging scanner type that is the most scattered. In comparison to the CNN feature representation, t-SNE results in SVM of the proposed YOLCO are clearly distributing in 7 clusters, against the ambiguous results by common CNNs. Positive slides and negative slides are gradually clustered more closer with classifiers from LSTM to Transformer in our method. In contrast, slides are hard to distinct even the classifier becoming more complex aside from S_4 type. Additionally, 3 positive and 3 negative slides are randomly selected based on the distribution of results of the proposed method in SVM to observe the separability, and every slide is moved into its true group in YOLCO via the most powerful Transformer.

5.4.3. Examples

The representative examples of two different frameworks are shown in Figure.7. There are three detectors used in our framework and their representative detection of above 6 slides are shown, where No. 6 belongs to S_1 , No. 1 and 2 belong to S_2 , No. 4 belong to S_3 , and No. 3 and 5 belong to S_4 .

In Figure.7 (b), we choose 4 of the intersection of top-100 detection results with the indication of their ranks. It is clear that YOLCO and YOLOv3 have a sufficient intersection, because they have similar accuracy in WSI classification and YOLCO has a slight superiority. However, ranks of the intersection are different. For instance, the highest detection result of YOLCO is ranked in the third place in No. 4 example, and negative cells are sorted ahead the positive cell. It is the reason why YOLOv3 gave a false prediction of No. 4 WSI. While Tiny usually output negative cells or artifacts, which are rarely existed in other better methods. That can explain why Tiny has a much lower accuracy than others.

5.5. Quantitative results at patch-level

5.5.1. Private data

For the private data, detection results of YOLO series and YOLCO are listed in Table.9. It is evident that the proposed CNN is performing a great mAP 72.5% and the best recall (Rec.) comparing with others. It shows a nice comparison with SOTA YOLOv3 with only $0.04\times \sim 0.08\times$ weighting in parameters and $1.0\% \sim 6.4\%$ decreasing in mAP.

5.5.2. Public data

For the public data, classification results of the best reported model VGG19, the SOTA model MNV2, and InCNet are listed in Table.9. The significance of our model can be proved by not only the best average accuracy (Acc.) 99.52% of all classes but also the best average sensitivity (Sens.) 99.84%.

5.5.3. Ablation studies: connecting methods

Ablation studies are accomplished to test the workability of connecting methods via changing the connectivity of Tiny, YOLCO, MNV2, and InCNet, which are based on the common convolution or the depthwise separable (DS) convolution. Note that "bl", in Figure 8 (a), is the baseline YOLCO that be without any connection, the "skip" connection is the skip/residual connection, and "half-InC" is the ablated version of the inline connection that only the first half groups are connected. And, in (b), different settings of n_g , the number of groups, show how the connectivity influences the classification performance.

Given curves in (a) that collected mAPs of validation data during the training phase of 6 CNNs reveal the model has a higher mAP with more connectivity. Especially, 67.4% and 69.3%, the lower mAPs of Tiny and bl which are non-connected, respectively, rising to 67.8% and 69.4%, the higher mAPs of Tiny+skip and bl+skip. In the meantime, except for the comparison between common convolutions from Tinys, bls are overfitted later and better with more connectivity, where skip < half-InC < InC = 72.5%, the best performance from the proposed method bl+InC. Additionally, the patch-level accuracy rising with more connectivity in (b) can further illustrate the performance of InCNet for cytopathology.

Table 7: Results per classifier: Classification performance on mixed scanners data (2,019 slides), where ‘‘Trans.’’ denotes Transformer model.

| | Tiny | | | MNv2 | | | YOLOv3 | | | YOLCO | | |
|--------|--------------|-------|-------|--------------|-------|-------|--------------|-------|-------|--------------|-------|-------|
| | Acc. | Sens. | Spec. | Acc. | Sens. | Spec. | Acc. | Sens. | Spec. | Acc. | Sens. | Spec. |
| SVM | 0.638 | 0.609 | 0.667 | 0.516 | 0.047 | 0.986 | 0.585 | 0.547 | 0.623 | 0.726 | 0.641 | 0.811 |
| RNN | 0.659 | 0.781 | 0.536 | 0.500 | 1.000 | 0.000 | 0.526 | 0.922 | 0.130 | 0.787 | 0.734 | 0.841 |
| LSTM | 0.653 | 0.828 | 0.478 | 0.500 | 1.000 | 0.000 | 0.787 | 0.922 | 0.652 | 0.745 | 0.766 | 0.725 |
| Trans. | 0.601 | 0.391 | 0.812 | 0.725 | 0.813 | 0.638 | 0.806 | 0.859 | 0.754 | 0.808 | 0.906 | 0.710 |

Table 8: Results of ablation study: Classification performance at the patch-level and the WSI-level. InCNet is set with $n_g = 8$ here, and P means the weight of parameters of network.

| | patch-level (1 st & 2 nd cohorts) | | | | WSI-level (1 st & 2 nd cohorts) | | | | WSI-level (ALL cohorts) | | | |
|-------|---|---------------------|---------------------|--|---|---------------------|---------------------|--|-------------------------|---------------------|---------------------|--|
| | InCNet | MNV2 | YOLO | YOLO | InCNet | MNV2 | YOLO | YOLO | InCNet | MNV2 | YOLO | YOLO |
| Loss | \mathcal{L}_{cls} | \mathcal{L}_{cls} | \mathcal{L}_{cls} | $\mathcal{L}_{cls} \& \mathcal{L}_{box}$ | \mathcal{L}_{cls} | \mathcal{L}_{cls} | \mathcal{L}_{cls} | $\mathcal{L}_{cls} \& \mathcal{L}_{box}$ | \mathcal{L}_{cls} | \mathcal{L}_{cls} | \mathcal{L}_{cls} | $\mathcal{L}_{cls} \& \mathcal{L}_{box}$ |
| P | 2.79M | 2.23M | 1.79M | 1.79M | 2.79M | 2.23M | 1.79M | 1.79M | 2.79M | 2.23M | 1.79M | 1.79M |
| Sens. | .957±.007 | .958±.006 | .820±.009 | .740±.014 | .825±.038 | .860±.037 | .625±.025 | .860±.049 | .664±.043 | .659±.129 | .709±.113 | .859±.040 |
| Spec. | .971±.004 | .961±.005 | .958±.008 | .970±.004 | .894±.015 | .764±.030 | .962±.039 | .909±.027 | .669±.058 | .739±.119 | .672±.121 | .693±.080 |
| Acc. | .964±.004 | .959±.004 | .889±.005 | .855±.006 | .860±.015 | .822±.009 | .794±.021 | .886±.013 | .667±.011 | .699±.017 | .691±.008 | .776±.030 |
| AUC | .964±.004 | .959±.004 | .889±.005 | .855±.006 | .890±.007 | .862±.009 | .801±.019 | .927±.011 | .692±.004 | .746±.018 | .750±.015 | .841±.030 |

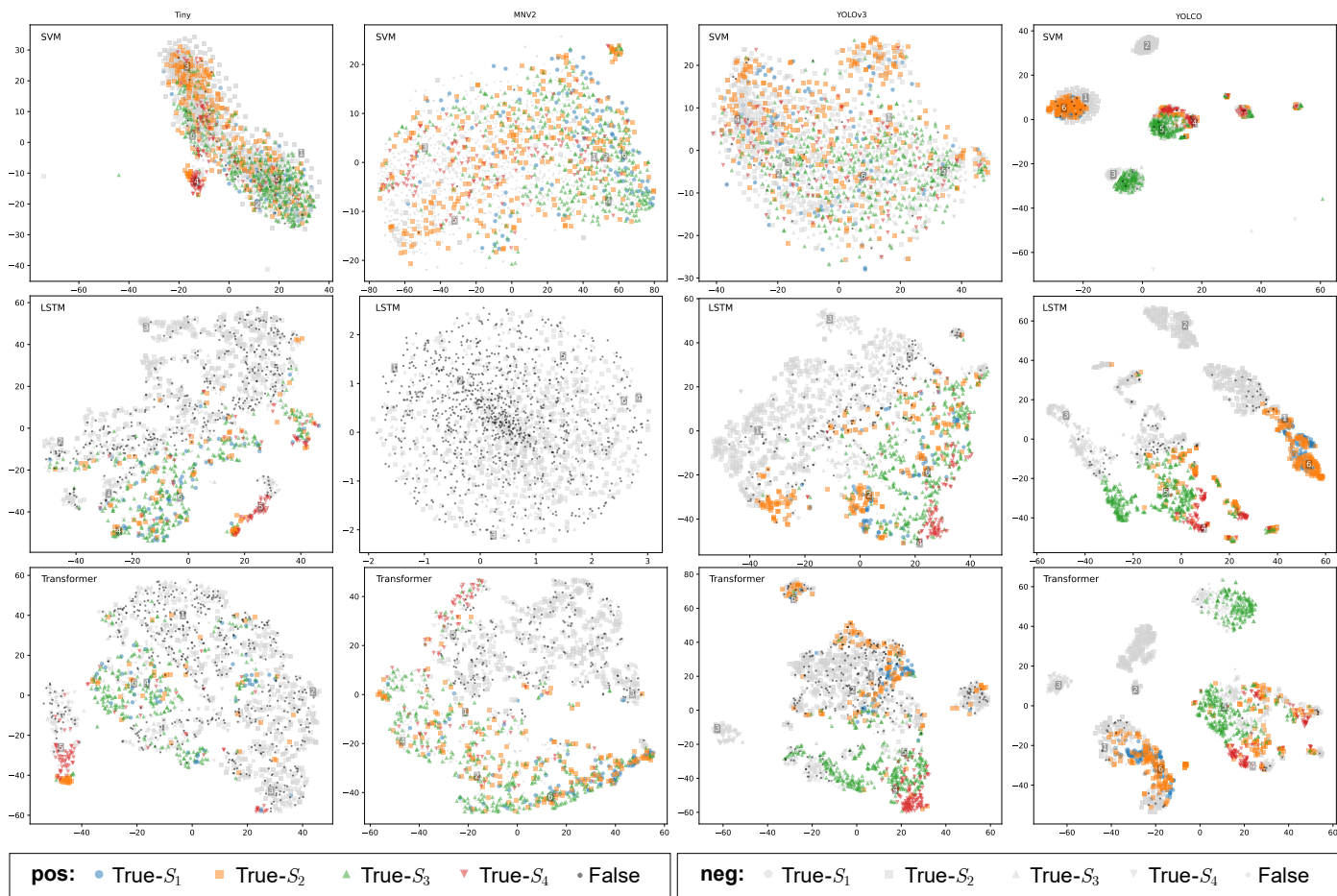


Fig. 6: Feature embedding from raw feature vectors (SVM), and embedded feature vectors (LSTM and Transformer) using t-SNE toolbox (Van der Maaten and Hinton (2008)).

5.6. C++ Deployment

Considering that the most efficient way to get computer-aided prediagnosis is to have a similar time cost between WSI computation and scanning. In python, our method is the fastest that needs 538.0s to compute one WSI, while the

second best YOLOv3 needs 1352.6s (the proposal is 2.51× faster). Although implementing the proposed method by python is friendly for showing and comparing the performance, the least time cost that is 538s per WSI is impractical. Thus, we release a C++ deployment of the proposed method in github to

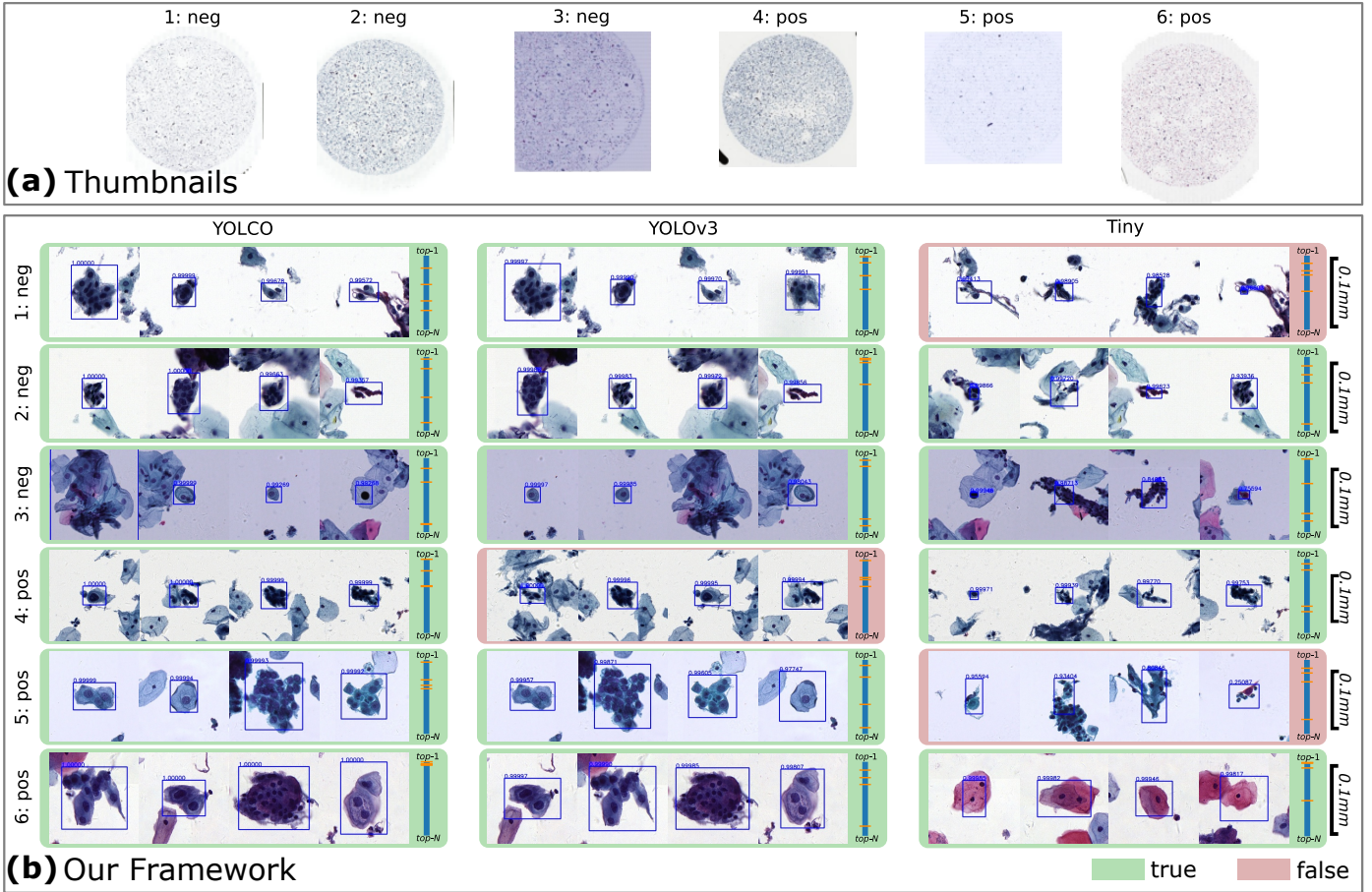


Fig. 7: 6 examples to illustrate the performance, where slides are chosen in t-SNE analysis (Figure.6), and "pos" denotes the positive diagnosis from the golden standard as well as "neg" denotes the negative diagnosis. (a) thumbnails at scale level 8 of 6 slides. (b) the intersection of 4 representative detection results between models under our framework, where Tiny usually performs different with others.

Table 9: Results on patch-level data: Detection performance on the private dataset $n = 19,974$. Classification performance on a public datasets by Plissiti *et al.* (2018), $n = 4,049$, where VGG19 is the best model of the literature.

| Private | Param. | mAP ₅ | Rec. | Prec. |
|-----------------------------------|--------|------------------|--------------|-------|
| YOLOv3 | 61.5M | <u>0.735</u> | 0.943 | 0.352 |
| Tiny | 8.67M | 0.674 | 0.919 | 0.261 |
| YOLOv3 | 1.79M | 0.725 | 0.955 | 0.215 |
| Public | | Acc. | Sens. | Spec. |
| VGG19 | 144M | .9950 | .9978 | .9938 |
| MNV2 | 2.23M | .9942 | .9981 | .9908 |
| InCNet _{n_g=8} | 2.79M | <u>.9952</u> | .9984 | .9922 |

Table 10: The practical speed of the proposed method after C++ deployment for two common WSI formats, SVS and MRXS. The release executable file is in github, where GMem denotes the GPU memory needing.

| | GMem | Speed _{s/WSI} | |
|-----------------|--------|------------------------|------|
| | | SVS | MRXS |
| Libtorch | 8.8 GB | 69.9 | 70.1 |
| Libtorch + half | 5.7 GB | 53.2 | 53.5 |

test the practical speed for application.

As listed in the Table.10, the proposed method is speeded up

to ~ 70 s per WSI whether it is SVS format or MRXS format after C++ deployment. It can be faster to ~ 53 s per WSI using half precision (single float precision).

The bottleneck of speeds in python is the limited multiple thread programming and the dynamic computation graph of Pytorch. In C++, we translate the python codes into an efficient multiple thread program, and generate the static computation graph from Pytorch model by using Libtorch, which is the official C++ deployment solution for Pytorch. Using 4 data loaders, the time cost of data loading is reduced to average ~ 100 ms per tile image. And, the model inference needs only ~ 1 s per tile image with the static computation graph.

6. Discussion

The effective computation has been mainly explored on pre-processing or postprocessing instead of the rethought of the backbone in the past. Applying the extraction for the foreground or the ROI before the CNN encoding, however, generally reduces the half pixels at most in our data. A highly integrated feature embedding is more efficient, and especially effective in the medical image field. According to this, recognizing ROI with the low magnification then sliding a small window of ROIs with the high magnification is the approach to represent

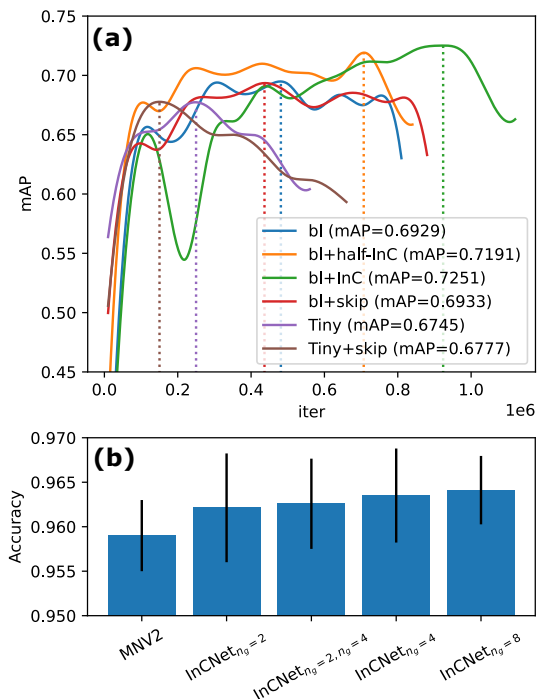


Fig. 8: Ablation studies for our inline connection at the patch-level. (a) The detection performance of proposed YOLCO (bl+InC) and its counterpart Tiny, where "half" denotes InC connected with only half of groups. (b) The classification performance of MNV2 and its varieties with the replacement of InverseResidual module by InCNet with the same channels, where the vertical line over the bar is the error bar from ten repeated runs, n_g is the group number, and the first four modules consist of fewer groups when n_g has two values.

the WSI by few small patch images. Some computations that are repeated for the same pixel with multiple models, however, are inevitable.

Thus, YOLCO (You Only Look Cytopathology Once) is proposed based on YOLOv3 in this study. It is the first time to represent a WSI via feature vectors corresponding to 32×32 small areas. In this new framework, effectiveness and efficiency are both improved. And, the fully convolutional structure of YOLCO with a light weight can avoid the same computation by extremely increasing the input size.

For encoding WSI by feature vectors, feature mixture are commonly and naturally established by the multi-task supervision for the CNN in one mixed loss function. Dual tasks, classification and location, in this study have a special function for the cytological data while the natural data does not have. That is the location annotation is more stable than the semantic based on the physical property.

It is reasonable that feature vectors of YOLCO with both semantic and location information are robust. The network for single task with a larger number of parameters can be well fitted at the patch-level just like upstream studies. Because the large amount of unseen data at the WSI-level, however, it will challenge the generalization of the model (the problem of the overfitting). So, when testing all WSIs, the trend of performance becomes opposite to that of patch-level. While the proposed YOLCO weakened the above effects because of the use of feature mixture by both classification and location tasks in

this downstream study, and always performs the best in different settings of the WSI dataset.

Otherwise, YOLCO is weak for the natural data. The comparison in the public MS COCO 2014, which has 40775 training images into 80 classes, is inconsistent with cytopathology:

| | Tiny | YOLOv3 | YOLCO |
|------------------|-------|--------|-------|
| mAP ₅ | 0.348 | 0.579 | 0.277 |

Dissimilar with the performance in the cervical data, the proposed YOLCO has a meagre performance in the natural dataset, 27.7% at mAP. It is not effective in such a complex upstream task because there are 80 classes and wider texture variety than the cytopathology. Not to mention the difficulty in overlapped objects and the depth of field, which are rare and slight in cytopathology.

7. Conclusion

In conclusion, the proposed YOLCO using the novel InC-Net module achieves a better WSI-level performance than the conventional framework and the SOTA model, while a slight loss occurs to the detection at the patch-level. Remarkably, the speed of YOLCO is faster and lighter than the SOTA CNNs and, meanwhile, the accuracy is better, which proves the workability and the efficiency of the proposed method via the simplified manner and the valid InCNet.

The experimental results further proved that well-designed models for the natural upstream task are improvable for the particular downstream task. Especially, the multi-connection between the different sizes of the receptive field inner the module can enrich the feature representation without any residual-like connections to deal with various complexities of cervical cells, while common CNNs prone to equally encode every pattern of the cervical cell image is inferior for the WSI-level analysis of cytopathology. It is reliable that the performance on the cervical data will be improved when the structure of the model can be further optimized according to our experiments. Moreover, the limited local annotation at the patch-level is relatively acceptable for multi-cohort and multiscale slides based on our feature mixture from the multiple task learning and the enhancement of the multi-scale inline connection.

Acknowledgments

The authors want to thank pathologists and organizations that provided the raw data and the manual annotations. As well as the Collaborative Innovation Center for Biomedical Engineering and the Britton Chance Center and MOE Key Laboratory for Biomedical Photonics should be greatly appreciated for their platforms and devices. This work is supported by the NSFC projects (grant 61721092) and the director fund of the WNLO.

References

- Bertram, C.A., Aubreville, M., Marzahl, C., Maier, A., Klopffleisch, R., 2019. A large-scale dataset for mitotic figure assessment on whole slide images of canine cutaneous mast cell tumor. *Scientific data* 6, 1–9.

- Bertram, C.A., Veta, M., Marzahl, C., Stathonikos, N., Maier, A., Klopfeisch, R., Aubreville, M., 2020. Are pathologist-defined labels reproducible? comparison of the tupac16 mitotic figure dataset with an alternative set of labels, in: *Interpretable and Annotation-Efficient Learning for Medical Image Computing*. Springer, pp. 204–213.
- Campanella, G., Hanna, M.G., Geneslaw, L., Miraflor, A., Silva, V.W.K., Busam, K.J., Brogi, E., Reuter, V.E., Klimstra, D.S., Fuchs, T.J., 2019. Clinical-grade computational pathology using weakly supervised deep learning on whole slide images. *Nature medicine* 25, 1301–1309.
- Cao, L., Yang, J., Rong, Z., Li, L., Xia, B., You, C., Lou, G., Jiang, L., Du, C., Meng, H., Wang, W., Wang, M., Li, K., Hou, Y., 2021. A novel attention-guided convolutional network for the detection of abnormal cervical cells in cervical cancer screening. *Medical Image Analysis* 73, 102197. URL: <https://www.sciencedirect.com/science/article/pii/S1361841521002425>, doi:<https://doi.org/10.1016/j.media.2021.102197>.
- Cheng, S., Liu, S., Yu, J., Rao, G., Xiao, Y., Han, W., Zhu, W., Lv, X., Li, N., Cai, J., et al., 2021. Robust whole slide image analysis for cervical cancer screening using deep learning. *Nature communications* 12, 1–10.
- Davey, E., Barratt, A., Irwig, L., Chan, S.F., Macaskill, P., Mannes, P., Saville, A.M., 2006. Effect of study design and quality on unsatisfactory rates, cytology classifications, and accuracy in liquid-based versus conventional cervical cytology: a systematic review. *The Lancet* 367, 122–132.
- Dong, N., Zhao, L., Wu, C., Chang, J., 2020. Inception v3 based cervical cell classification combined with artificially extracted features. *Applied Soft Computing* 93, 106311.
- Dov, D., Kovalsky, S.Z., Assaad, S., Cohen, J., Range, D.E., Pendse, A.A., Henao, R., Carin, L., 2021. Weakly supervised instance learning for thyroid malignancy prediction from whole slide cytopathology images. *Medical Image Analysis* 67, 101814.
- Gao, S.H., Cheng, M.M., Zhao, K., Zhang, X.Y., Yang, M.H., Torr, P., 2021. Res2Net: A New Multi-Scale Backbone Architecture. *IEEE TRANSACTIONS ON PATTERN ANALYSIS AND MACHINE INTELLIGENCE* 43, 652–662. doi:{10.1109/TPAMI.2019.2938758}.
- Gupta, M., Das, C., Roy, A., Gupta, P., Pillai, G.R., Patole, K., 2020. Region of interest identification for cervical cancer images, in: *2020 IEEE 17th International Symposium on Biomedical Imaging (ISBI)*, IEEE. pp. 1293–1296.
- He, K., Zhang, X., Ren, S., Sun, J., 2016. Deep residual learning for image recognition, in: *Proceedings of the IEEE conference on computer vision and pattern recognition*, pp. 770–778.
- Howard, A.G., Zhu, M., Chen, B., Kalenichenko, D., Wang, W., Weyand, T., Andreetto, M., Adam, H., 2017. Mobilenets: Efficient convolutional neural networks for mobile vision applications. arXiv preprint arXiv:1704.04861.
- Jantzen, J., Norup, J., Dounias, G., Bjerregaard, B., 2005. Pap-smear benchmark data for pattern classification. *Nature inspired Smart Information Systems (NiSIS 2005)*, 1–9.
- Liang, Y., Tang, Z., Yan, M., Chen, J., Liu, Q., Xiang, Y., 2021. Comparison detector for cervical cell/clumps detection in the limited data scenario. *Neurocomputing* 437, 195–205.
- Lin, H., Chen, H., Wang, X., Wang, Q., Wang, L., Heng, P.A., 2021. Dual-path network with synergistic grouping loss and evidence driven risk stratification for whole slide cervical image analysis. *Medical Image Analysis* 69, 101955.
- Lin, T.Y., Goyal, P., Girshick, R., He, K., Dollár, P., 2017. Focal loss for dense object detection, in: *Proceedings of the IEEE international conference on computer vision*, pp. 2980–2988.
- Litjens, G., Bandi, P., Ehteshami Bejnordi, B., Geessink, O., Balkenhol, M., Bult, P., Halilovic, A., Hermesen, M., van de Loo, R., Vogels, R., et al., 2018. 1399 h&e-stained sentinel lymph node sections of breast cancer patients: the camelyon dataset. *GigaScience* 7, giy065.
- Liu, Y., Gadepalli, K., Norouzi, M., Dahl, G.E., Kohlberger, T., Boyko, A., Venugopalan, S., Timofeev, A., Nelson, P.Q., Corrado, G.S., et al., 2017. Detecting cancer metastases on gigapixel pathology images. arXiv preprint arXiv:1703.02442.
- Lu, Z., Carneiro, G., Bradley, A.P., Ushizima, D., Nosrati, M.S., Bianchi, A.G., Carneiro, C.M., Hamarneh, G., 2016. Evaluation of three algorithms for the segmentation of overlapping cervical cells. *IEEE journal of biomedical and health informatics* 21, 441–450.
- Van der Maaten, L., Hinton, G., 2008. Visualizing data using t-sne. *Journal of machine learning research* 9.
- Nayar, R., Wilbur, D.C., 2017. The bethesda system for reporting cervical cytology: a historical perspective. *Acta cytologica* 61, 359–372.
- Otsu, N., 1979. A threshold selection method from gray-level histograms. *IEEE transactions on systems, man, and cybernetics* 9, 62–66.
- Plissiti, M.E., Dimitrakopoulos, P., Sfikas, G., Nikou, C., Krikoni, O., Charchanti, A., 2018. Sipakmed: A new dataset for feature and image based classification of normal and pathological cervical cells in pap smear images, in: *2018 25th IEEE International Conference on Image Processing (ICIP)*, IEEE. pp. 3144–3148.
- Redmon, J., Farhadi, A., 2017. Yolo9000: better, faster, stronger, in: *Proceedings of the IEEE conference on computer vision and pattern recognition*, pp. 7263–7271.
- Redmon, J., Farhadi, A., 2018. Yolov3: An incremental improvement. arXiv preprint arXiv:1804.02767.
- Ren, S., He, K., Girshick, R., Sun, J., 2015. Faster r-cnn: Towards real-time object detection with region proposal networks, in: *Advances in neural information processing systems*, pp. 91–99.
- Sandler, M., Howard, A., Zhu, M., Zhmoginov, A., Chen, L.C., 2018. Mobilenetv2: Inverted residuals and linear bottlenecks, in: *Proceedings of the IEEE conference on computer vision and pattern recognition*, pp. 4510–4520.
- Saslow, D., Solomon, D., Lawson, H.W., Killackey, M., Kulasingam, S.L., Cain, J., Garcia, F.A., Moriarty, A.T., Waxman, A.G., Wilbur, D.C., et al., 2012. American cancer society, american society for colposcopy and cervical pathology, and american society for clinical pathology screening guidelines for the prevention and early detection of cervical cancer. *CA: a cancer journal for clinicians* 62, 147–172.
- Sung, H., Ferlay, J., Siegel, R.L., Laversanne, M., Soerjomataram, I., Jemal, A., Bray, F., 2021. Global cancer statistics 2020: Globocan estimates of incidence and mortality worldwide for 36 cancers in 185 countries. *CA: A Cancer Journal for Clinicians* eprint, eprint. doi:<https://doi.org/10.3322/caac.21660>.
- Tan, X., Li, K., Zhang, J., Wang, W., Wu, B., Wu, J., Li, X., Huang, X., 2021. Automatic model for cervical cancer screening based on convolutional neural network: a retrospective, multicohort, multicenter study. *Cancer Cell International* 21, 1–10.
- Tareef, A., Song, Y., Huang, H., Wang, Y., Feng, D., Chen, M., Cai, W., 2017. Optimizing the cervix cytological examination based on deep learning and dynamic shape modeling. *Neurocomputing* 248, 28–40.
- Vaswani, A., Shazeer, N., Parmar, N., Uszkoreit, J., Jones, L., Gomez, A.N., Kaiser, L., Polosukhin, I., 2017. Attention is all you need. arXiv preprint arXiv:1706.03762.
- Xiang, Y., Sun, W., Pan, C., Yan, M., Yin, Z., Liang, Y., 2020. A novel automation-assisted cervical cancer reading method based on convolutional neural network. *Biocybernetics and Biomedical Engineering* 40, 611–623.
- Yao, J., Zhu, X., Jonnagaddala, J., Hawkins, N., Huang, J., 2020. Whole slide images based cancer survival prediction using attention guided deep multiple instance learning networks. *Medical Image Analysis* 65, 101789.
- Yu, S., Zhang, S., Wang, B., Dun, H., Xu, L., Huang, X., Shi, E., Feng, X., 2021. Generative adversarial network based data augmentation to improve cervical cell classification model. *Mathematical Biosciences and Engineering: MBE* 18, 1740–1752.
- Zhang, L., Kong, H., Ting Chin, C., Liu, S., Fan, X., Wang, T., Chen, S., 2014. Automation-assisted cervical cancer screening in manual liquid-based cytology with hematoxylin and eosin staining. *Cytometry Part A* 85, 214–230.
- Zhang, L., Lu, L., Nogue, I., Summers, R.M., Liu, S., Yao, J., 2017. Deepapp: deep convolutional networks for cervical cell classification. *IEEE journal of biomedical and health informatics* 21, 1633–1643.
- Zhao, Z., Lin, H., Chen, H., Heng, P.A., 2019. Pfa-scannet: pyramidal feature aggregation with synergistic learning for breast cancer metastasis analysis, in: *International Conference on Medical Image Computing and Computer-Assisted Intervention*, Springer. pp. 586–594.
- Zhu, X., Li, X., Ong, K., Zhang, W., Li, W., Li, L., Young, D., Su, Y., Shang, B., Peng, L., et al., 2021. Hybrid ai-assistive diagnostic model permits rapid tbs classification of cervical liquid-based thin-layer cell smears. *Nature Communications* 12, 1–12.